Nanoscale Advances

ROYAL SOCIETY OF CHEMISTRY

PAPER

View Article Online
View Journal | View Issue

Cite this: *Nanoscale Adv.*, 2025, **7**, 4336

Gold-doped wollastonite nanohybrids enhance bone regeneration *via* the bone morphogenetic protein-2, SMAD1, and Runt-related transcription factor-2 signalling pathway

Mona Moaness,*[a] Ahmed N. Emam,*[ab] Abeer Salama,[c] Manar M. Ahmed,[d] Esmat M. A. Hamzawy,[d] Areg E. Omar[e] and Gehan T. El-Bassyouni[a]

This study examines the prospect of bone regeneration using pure wollastonite and gold-doped wollastonite nanohybrids prepared using a wet chemical method. After four weeks of soaking in simulated body fluid, the bio-mineralization of wollastonite was accelerated, with excellent apatite layer deposition accomplished at varying ratios (*i.e.* 0, 1.25, 2.5, 5, and 7.5 wt/v%). The *in vitro* biodegradation and swellability of the prepared composites revealed controlled and stable bone defect behavior, with enhanced adequate swellability. W/Au 5 wt/v% demonstrated the highest potential for water absorption, amounting to approximately 80–85%. X-ray photoelectron spectroscopy analysis confirmed the composition of the $CaSiO_3$ sample for pure wollastonite while showing that gold nanoparticles or a thin layer of gold was deposited on the surface of $CaSiO_3$ in the case of the gold-doped wollastonite nanohybrid (7.5 wt/v%). The mechanical strength increased considerably with gold nanoparticle doping. *In vivo* bone osteogenesis was assessed in a rat femur bone defect model to demonstrate the bone regeneration ability of the fabricated nanocomposites. Results showed up-regulation of the osteogenic markers, including bone morphogenetic protein 2 (Bmp2), Smad1, and Runx2 signalling, which is involved in osteoblast differentiation. Enhanced alkaline phosphatase (ALP) activity, which affects the mineralization ability of cells, was also evaluated. Furthermore, gold nanoparticle doping reduced glycogen synthase kinase-3β (GSK 3β) levels compared to the positive control, which stimulated bone formation and increased bone mineral density (BMD) after 2 months of implantation. These results aligned with histopathological studies that showed increased osteoblast proliferation and blood vessel regeneration. The findings demonstrate that wollastonite nanohybrids, both pure and gold-doped, show promise as materials for bone replacement and regeneration applications.

Received 21st February 2025
Accepted 20th May 2025

DOI: 10.1039/d5na00176e

rsc.li/nanoscale-advances

1. Introduction

Bone abnormalities caused by trauma, tumor removal, or congenital abnormalities are a big challenge in orthopaedic medicine and require advanced biomaterial solutions for effective regeneration. Although many synthetic materials have been explored for bone tissue engineering, the development of bioactive nanocomposites that can effectively stimulate osteogenesis while maintaining structural integrity remains a critical area of research.[1,2] Recent advances in materials science have highlighted the potential of wollastonite (W)-based ceramics, especially when enhanced with noble metal nanoparticles, as promising candidates for bone tissue regeneration.[3–6]

Bone metabolism depends on the dynamic equilibrium of homeostasis and the maintenance of cells such as osteoclasts and osteoblasts.[7] Bone metabolism homeostasis is a complex process involving hormone secretion, aging, calcium malabsorption, nutrition and disease-related damage. Wollastonite (W), an analogue of the natural mineral calcium silicate,[8] is used as a common biological filler for ceramic grafts used in bone reconstructive and regenerative surgery in dentistry, orthopaedic, maxillofacial plasty, and other fields. Wollastonite (W)'s hydrophilic character aids in the development of an appetite layer on its surface in the bioorganic medium, where

[a]*Refractories, Ceramics and Building Materials Department, Advanced Materials Technology & Mineral Resources Research Institute, National Research Centre (NRC), 33 El Bohouth St., Dokki, Cairo, P. O. Box 12622, Egypt. E-mail: drmonabiomaterials@gmail.com; ahmed.gsc.ndp@gmail.com; an.emam@nrc.sci.eg*

[b]*Nanomedicine & Tissue Engineering Research Lab, Medical Research Centre of Excellence, National Research Centre, 33 El Bohouth St., Dokki, Cairo, P. O. Box 12622, Egypt*

[c]*Pharmacology Department, Medical Research and Clinical Studies Institute, National Research Centre, 33 El Bohouth St., Dokki, Cairo, PO Box 12622, Egypt*

[d]*Glass Research Department, National Research Centre, 33 El-Bohouth St., Dokki, Cairo, P.O. Box 12622, Egypt*

[e]*Department of Physics, Faculty of Science, Al-Azhar University, (Girls Branch), Cairo, P.O Box 11884, Egypt*

an active ion outflow (exchange) of Ca^{2+} and SiO_3^{2-} occurs. These ions have been shown to regulate key bone tissue markers by controlling gene expression, cell differentiation, and cell growth. The affected markers include osteocalcin, BMP-2, RUNX2, transforming growth factor-beta (TGF-β), and alkaline phosphatase (ALP).[9] In addition to being involved in extracellular matrix production, silica ions are essential for the activation and deactivation of mitogen-activated protein kinase (MAPK) and the p38 MAP Kinase (MAPK) signaling pathway. Additionally, wollastonite (W) controls the immunological regulation of inflammation by inhibiting nuclear factor NF-κB transcription and MAPK signaling, as well as by triggering macrophage apoptosis *via* a caspase-dependent route.[10] The bioactive qualities of wollastonite (W), which stimulate osteoinduction and osteogenesis and bind with bone tissue through a process known as binding osteogenesis, are provided by the ingredients listed. Biswas *et al.* conducted a thorough analysis of scholarly works devoted to wollastonite's biocompatible qualities.[11] It is possible to obtain synthetic wollastonite (W) with the required physical–mechanical characteristics, including the volume porosity type and shape, surface morphology (roughness and curvature), dispersiveness, and particle crystallinity shape, in addition to bioactive characteristics like bio-resistance.[12]

Gold nanoparticle (Au-NPs)-containing bio-composite materials is an intriguing prospect. Numerous investigations into the antibacterial, antimicrobial, antifungal, and anti-inflammatory activities of Au-NPs in polarizing cells of innate immunity have demonstrated their beneficial significance. Unique functional systems for biomedicine can be created by combining the characteristics with bioactive capabilities in the creation of biocomposites made of Au-NPs. A more intriguing aspect of these composites is their specific interactions with immune cells (neutrophils, macrophages), which may favorably affect the osteogenesis process in bone tissue regeneration.[13]

The BMP-2/Smads/RUNX2 pathway plays a fundamental part in bone growth and osteoblast differentiation *via* a complex molecular mechanism. Therefore, BMP-2 triggers the pathway by binding to its receptors; this results in the phosphorylation of receptor-regulated Smads, especially Smad1/5/8; after that, these Smads always combine with Smad4 and translocate to the nucleus.[14,15] These active Smad complexes are directly regulated at the transcriptional level, the expression and activity of RUNX2, considered a master transcription factor for osteoblast differentiation, while controlling the manifestation of essential osteoblast-specific genes such as osteocalcin, bone sialoprotein, and type I collagen.[16,17] This pathway is essential for both embryonic skeletal development and adult bone homeostasis because it coordinates the differentiation of mesenchymal stem cells into functional osteoblasts and subsequent bone matrix mineralization.[18,19]

Bioactive and osteoconductive wollastonite, which is a type of calcium silicates widely used in dentistry and bone tissue engineering, contains calcium ions that mediate metabolic responses in bone regeneration, while silicon ions help with early stages of calcification, cell attachment and angiogenesis through activation of molecular signaling pathways: BMP-2/Smad/RUNX2 pathway, which is crucial for: osteoblast differentiation, and bone formation.[20] Calcium activates various pathways through calcium-sensing receptors. These calcium silicates can be improved by adding various elements like strontium, lithium, magnesium, manganese, copper, gadolinium, zinc, and lanthanum, which improve osteoblastic differentiation and mechanical resistance, bone and cartilage regeneration, and bone formation and vascularization.[21,22]

By altering cellular signaling pathways through interactions with cytosolic proteins, Au-NPs have been demonstrated to greatly increase induced osteogenic activity and osteoblast mineralization. Cells treated with Au-NPs showed mineralized nodule growth, a significant increase in ALP activity induced by mechanical stress, and up-regulation of the lineage commitment gene Runx2, in addition to other osteogenic markers (BMP1, BMP2, BMP4, OCN, and Col1a2). Furthermore, Au-NPs stimulate the signaling pathways of RUNX2, Wnt/β-catenin, MAPK38/RUNX2, and mechanical stimuli-responsive cells to promote osteogenic differentiation of MSCs. In rabbit calvarial defects, Yes-associated protein (Yap) activity increases ALP and RUNX2 levels and accelerates mineralization and the production of new bone.[23,24] Au-NPs block osteoclast activity and stimulate osteogenic differentiation, which has an impact on bone regeneration.[25] In addition, previous studies have examined the capacity of Au-NPs to promote bone regeneration, and they are currently being investigated for the treatment of osteoporosis.[25]

The preparation of wollastonite gold-doped nanoparticles and the detection of osteogenesis following the implantation of a nanocomposite in a bone defect using bone morphogenetic protein 2 (Bmp2)/Smads 1/Runx2 Pathway biomarkers and ALP detection for the first time are novel aspects of this study. Consequently, this study's objective was to assess the potential of new gold-doped wollastonite nanocomposites to promote bone regeneration in femoral lesions *in vivo*. The intended research was accomplished by studying the *in vitro* biomineralization and biodegradation of the prepared nanocomposites, as well as the measurement of osteogenic biomarkers following the treatment of femoral bone defects using our manufactured nanocomposites linked to bone mineral density and evaluation of histopathological studies.

2. Experimental

2.1. Materials

Alkaline phosphatase (ALP) was obtained from Bio Diagnostic Co., Egypt. Bmp-2, Runx2, Smad1 and Glycogen Synthase Kinase-3β (GSK-3β) enzyme-linked immune-sorbent assay (ELISA) kits were obtained from SunLong Biotechnology Co. Ltd, China. The additional chemicals were all classified as analytical grade. Nitric acid (HNO_3) and Calcium carbonate ($CaCO_3$) were purchased from El-Gomhouria Company, Cairo, Egypt. Amorphous silica (SiO_2Gel, FlukaChemie GmbH, Switzerland), an inorganic compound [gold chloroauric acid ($HAuCl_4 \cdot 3H_2O$, BDH, England)], and tri-sodium citrate dehydrate ($C_6H_5Na_3O_7 \cdot 2H_2O$, Honeywell, USA).

2.2. Fabrication of wollastonite and gold-doped wollastonite nanohybrids

Pure wollastonite (W) and gold-doped wollastonite (W/Au) were synthesized using a wet chemical technique, as reported by Emam *et al.*[3] The compositions were formulated with $CaSiO_3$: Au ratios of 100 : 0, 98.75 : 1.25, 97.5 : 2.5, 95 : 5, and 92.5 : 7.5, corresponding to W/Au0, W/Au1.25, W/Au2.5, W/Au, and W/Au7.5 wt/v%, respectively (Table 1). The synthesis of α-wollastonite involved using calcium carbonate ($CaCO_3$) as a source of CaO and amorphous silica as a SiO_2 source. Specifically, 84.42 g of $CaCO_3$ was dissolved in 200 mL of nitric acid (HNO_3) to convert $CaCO_3$ into water-soluble calcium nitrate [$Ca(NO_3)_2$]. Subsequently, 51.72 g of a water-soluble SiO_2 gel was mixed thoroughly with the resulting Ca $(NO_3)_2$ solution at room temperature. After 24 hours of incubation at 100 °C, the mixture was calcined for two hours at 1200 °C.

Gold-doped wollastonite (W/Au) nanohybrids were fabricated under the same conditions with the addition of a colloidal aqueous solution of Au nanoparticles (Au-NPs) at specified W/Au wt/v% ratios. This mixture of $Ca(NO_3)_2$ and SiO_2 gel, with the Au-NPs incorporated, was incubated at 100 °C for 24 hours and subsequently calcined at 1200 °C for 2 hours, resulting in the formation of gold-doped wollastonite (W/Au), as detailed in Table 1.

2.3. X-ray photoelectron spectroscopy (XPS) technique

The XPS measurements were conducted using an Al K monochromatic radiation source with an energy of 1486.7 eV. A hemispherical analyzer was used in conjunction with a SPECS spectrometer, specifically the XR-50 source with a monochromator (FOCUS 600). The ultrahigh vacuum (UHV) reached a pressure of 1109 mbar. The pressure achieved in the ultrahigh vacuum (UHV) test was 1109 mbar. The data for quantitative analysis were analyzed using Casa XPS processing and ULVAC-PHI MultiPak software (ver. 9.0.1, Osaka, Japan). The XPS spectra of Pure W and the W/Au nanohybrid were obtained using a PHOIBOS 150 MCD NAP instrument.

2.4. Mechanical properties

The compressive strength of the synthesized nanocomposites was evaluated to determine their mechanical behavior. Various nanopowders were used to form cylindrical specimens that were 12 mm in diameter and 11 mm in height. The ends of the specimens were polished to obtain a smooth and level surface for accurate testing. The compressive strength measurements were performed in agreement with the ASTM C1424 standards using a universal multi-testing machine (Tinius Olsen 25ST, UK) operating at a crosshead speed of 0.5 mm min^{-1}. Three replicate specimens of each composition were exposed to testing to ensure reliable data.

Table 1 Compositions of pure (W) and gold-doped (W/Au) wollastonite nanohybrids[a]

Symbol	Composition
W	Pure wollastonite (100 : 0)
W/Au 1.25	W/Au: 1.25 wt/v% (98.75 : 1.25 gold nanoparticles)
W/Au 2.5	W/Au: 2.5 wt/v% (97.5 : 2.5 gold nanoparticles)
W/Au 5	W/Au: 5 wt/v% (95 : 5 gold nanoparticles)
W/Au 7.5	W/Au: 7.5 wt/v% (92.5 : 7.5 gold nanoparticles)

[a] W: wollastonite, W/Au: gold-doped wollastonite nanohybrid, wt/v%: weight per volume ratio.

2.5. *In* vitro studies

2.5.1. Biomineralization assessment. Using the technique described by Kokubo *et al.*, the bioactivity of the disc samples was assessed *in vitro* for 2 weeks and 1 month using simulated body fluid (SBF).[26] The discs were placed in sterile containers with a controlled SBF-to-disc weight ratio to ensure consistency. The container was closed and incubated at 37 °C for 14 days. When the immersion period was over, the samples were removed, washed with deionized water and 100% ethanol to remove any remaining fluid, and allowed to air dry at room temperature.[27] Surface chemical changes, along with microstructural and morphological variances post-immersion, were analyzed using scanning electron microscopy (SEM) coupled with energy-dispersive X-ray spectroscopy (EDX).

2.5.2. Biodegradation, ion release and pH evaluation. Wollastonite (W) and gold-doped wollastonite nanohybrids (W/Au) were evaluated for swellability and bone defect behavior using an initial weight of 0.5 g. Thereafter, the sample was immersed in 50 mL SBF (pH 7.4) at 37 °C in a sterilized closed Falcon tube at predetermined times (1, 3, 7, 10, 14 and 30 days). After removing the SBF, the samples were weighed and their wet weight was determined. After a one-hour drying period in an oven dryer, the samples were weighed once more to determine their dry weight. Eqn (1) and (2) were used to calculate the weight loss percentage and/or water absorption percentage (swellability %):

$$\text{Weight loss (erosion behaviour)}\% = \frac{W_i - W_d}{W_i} \times 100 \quad (1)$$

$$\text{Water adsorption(swellability)}\% = \frac{W_w - W_d}{W_d} \times 100 \quad (2)$$

where W_i, W_d and W_w are the initial weight, dry weight and wet weight of the nanoparticles, respectively.

The pH values and concentrations of ions released from pure wollastonite and gold-doped nanoparticles into the solution were determined to assess the effect of gold nanoparticle addition on wollastonite dissolution. The dissolution test was conducted in simulated body fluid (SBF). SBF was prepared according to Kokubo and Takadama.[26] The composition and ionic concentration of this agent is similar to those of human blood plasma. The inorganic ion concentrations in SBF were Na^+ 142.0 mM, K^+ 5.0 mM, Ca^{2+} 2.5 mM, Mg^{2+} 1.5 mM, Cl^-148.0 mM, HCO^{3-}4.2 mM, $HPO_4{}^{2-}$1.0 mM, $SO_4{}^{2-}$0.5 mM. The solution was buffered at pH 7.4 with tris(hydroxymethyl) aminomethane and 1 M HCl at 37 °C.

The collected solution's pH was determined. Eventually, the entire solution was eliminated and replaced with a fresh one. Up until measurement, the gathered solutions were kept at −20 °C. Using a chemical kit and colorimetric methods, the

concentrations of Ca and P released from the wollastonite into solutions were evaluated. A UV/visible spectrometer (model SP-2000UV) was used to measure ion concentrations at wavelengths of 340 and 612 nm, respectively. An inductively coupled plasma emission spectrometer (model 720 ICP-OES, Agilent Technologies) was used to measure the amounts of Si^{4+} and Au^{3+} ions.

2.6. *In vivo* studies

2.6.1. Animals. Adult male Wistar albino rats weighing 140–160 g were provided by the animal house at the National Research Centre (NRC), Cairo, Egypt. Rats were housed under 12-hours light/dark cycles at a regulated temperature (22-25 °C), with unlimited access to tap water and a standard diet. The study methods were conducted in accordance with the ethical guidelines for the care and use of experimental animals that were authorized by the NRC's Medical Research Ethics Committee (MREC) (approval number 02540223), and all animals received human care.

2.6.2. Experimental design

2.6.2.1. Animal surgical procedure. For short-term anesthesia, animals were anesthetized using sodium thiopental–xylazine (40 mg kg^{-1} sodium thiopental, IP, and 10 mg kg^{-1} xylazine, IM).[28] The surgical site was shaved and prepared with a solution of betadine (povidone–iodine) and alcohol. The skin over each femoral diaphysis was incised under sterile surgical conditions, and the skin, muscles and ligaments were retracted so that the femur bone can be exposed. A mid-shaft femoral cortical bone defect (3 mm in diameter) was created in each femur using a low-speed dental burr and washed with sterile saline solution to avoid overheating and additional bone damage.[29] Gauze was used to control bleeding at the surgical site. The grafting materials were added in sufficient quantity to fill the holes, and layers of sutures were applied to the skin, muscles, and periosteum. The animals were given an antibiotic (gentamicin, 2 mg kg per B wt, IM) and ketoprofen (5 mg kg per B wt, SC) for 3 days post-surgery.[30] Finally, the animals were slaughtered for evaluation at the end of the definite period, and two femurs of each rat were used; thus, each grafting material had eight to ten defects. Each animal was closely monitored for any local or general complications after the operation and during the scheduled experimental period.

Rats were categorized randomly into 7 main groups; each group included 10 albino rats divided into 2 subgroups; each subgroup consists of 5 rats, as follows: Group 1: normal control group (group of healthy bone), Group 2: positive control group (empty defects without any grafting material), Group 3: base (W; not contain any Au-NPs), Group 4: W/Au 1.25 wt/v% group, Group 5: W/Au 2.5 wt/v% group, Group 6: W/Au 5 wt/v% group, and Group 7: W/Au 7.5 wt/v% group. The first subgroup was sacrificed after one month of the experiment, and the second subgroup was sacrificed after two months of operation. (*i.e.*, the *in vivo* protocol had two postoperative periods, 1 and 2 months).

2.6.2.2. Biochemical analysis

2.6.2.2.1 Blood sample preparation. At 1 and 2 months after surgery, heparinised capillary tubes were used to extract blood from the retro-orbital venous plexus while the patient was under anaesthesia. Samples of blood were centrifuged at 3000 rpm for 10 minutes.[31] For ALP analysis, serum samples were kept at −20 °C. Under pentobarbital sodium anaesthesia (40 mg kg^{-1}, i.p.), rats were sacrificed by cervical dislocation, and the bones ($n = 6$) were dissected and weighed independently. Using a homogenizer (Heidolph Co., DIAX 900, and Germany), the bones of each rat were homogenized in an ice-cold phosphate buffer (pH 7.4) to create a 20% (w/v) homogenate. For the biochemical examination of Bmp-2, Runx2, Smad 1, and GSK-3β, homogenates were centrifuged at 3000 rpm for 10 minutes at 4 °C and then kept at −80 °C.[32]

Alkaline phosphatase (ALP) activity (osteogenic activity). ALP activity was measured using an Alkaline Phosphatase Assay Kit (Biodiagnostic), diagnostic and research reagents (Egypt) according to the manufacturer's protocol for serum samples. In such cases, the blood serum samples were diluted using a dilution factor of 1 : 1 with either normal saline (0.9% NaCl) or PBS (0.01 M, pH 7.4). To begin the analysis, add 5 μL of standard to 5 μL of sample to the corresponding sample wells. Next, add 25 μL of working solution to each well and mix thoroughly for 10 seconds using a microplate reader. Incubate the plate at 37 °C for 30 minutes. After incubation, add 100 μL of alkali reagent followed by 150 μL of chromogenic agent to each well, then mix thoroughly for 10 seconds using the microplate reader. The assay was based on the ALP's capacity to cleave the phenyl phosphate group into phenol and phosphate, and the liberated phenol was measured colorimetrically in the presence of 4-aminophenazone and potassium ferricyanide at 510 nm using a microplate reader FLUOstar OPTIMA (BMG LABTECH GmbH, Ortenberg, Germany).

Using ELISA kits, the bone contents of Bmp-2, Runx2, and Smad 1 were observed. We calculated the results according to the manufacturer's guidelines. Each parameter's immobilized antibodies were added to the wells holding the standards and samples, along with horseradish peroxidase-conjugated streptavidin. The wells were then aspirated and cleaned five times with the kit washing solution after incubation for 60 minutes at 37 °C. After filling the wells with chromogen, A and B solutions, they were incubated at 37 °C for 15 minutes. Bmp-2, Runx2, and Smad 1 binding amounts were represented by the color that emerged. At 450 nm, color intensity was assessed after 10 minutes.[33]

2.6.3. Dual energy X-ray absorptiometry (DEXA). The bone mineral density (BMD) test is used to assess bone diseases, such as osteoporosis. Immediately after euthanasia, the region corresponding to the 5-mm femur defect (as created at the time of surgery) in the coronal plane was scanned using A dual X-ray absorptiometry (DEXA) (Norland Medical Systems Inc., XR-46, Fort Atkinson, Wisconsin, Model 434 A063, USA) for BMD analysis. Three bone samples were analyzed concurrently in the same scan. analysis (QDR 2000 Hologic, Bedford, MA, USA). The standardized position of the defect was ensured to achieve consistency in the positioning of the region under examination. Bone mineral and corresponding density were calculated using a high-resolution software algorithm for small animals supplied by the manufacturer.

2.6.4. Histopathological study. Shortly after sacrifice, the femurs of each rat were dissected ($n = 4$), washed thoroughly with normal saline and fixed in 10% neutral buffered formalin for 72 h. After being cleaned for 30 minutes with tap water, each specimen was dehydrated in increasing grades of absolute alcohol (70%, 90%, and 95%), clarified in xylene, and finally embedded in paraffin wax. Histopathological analysis was performed by cutting and staining 6 μm thick serial sections with hematoxylin and eosin (H & E).

2.7. Statistical analysis

The standard deviation (S.D.) ± mean was used to present the results. Fisher's LSD post-hoc test for means comparison was used after one-way analysis of variance (ANOVA) was used to estimate the data using GraphPad Prism software, version 5 (GraphPad Co., San Diego, USA). A difference of $p < 0.05$ was considered significant.

3. Results and discussion

3.1. X-ray photoelectron spectroscopy measurements

Elemental compositions using X-ray photoelectron spectroscopy (XPS) for pristine wollastonite (W) and gold-doped wollastonite (W/Au) with a ratio of 7.5 wt/v% Au-NPs are shown in Fig. 1 and 2, respectively. Fig. 1a shows the survey spectrum of pristine wollastonite (W) in which O 1 s, C 1 s, Ca 2p, Si 2p, and Si 2 s orbital peaks appear.[31] This overview confirms the incidence of expected elements in the sample. Moreover, Fig. 1b shows a high-resolution Ca 2p spectrum displaying a doublet structure typical of Ca 2p at 348.4 eV (2p 1/2) and 352.23 eV (2p 3/2).[32–34] The splitting of these peaks agrees with spin–orbit coupling in calcium. The high-resolution XPS spectrum of the Si 2s spectrum is shown in Fig. 1c. The main peak is centered at a binding energy level of 155.85 eV and could be assigned to Si–O bonds, as in silicates; other peaks at lower binding energy values of 153.89 eV and 152.43 eV indicate the presence of the Si–Si bonds, signifying the existence of some elemental silicon or silicon clusters in the sample.[34,35] Likewise, Fig. 1d shows the de-convolution of the O 1s XPS spectrum into three components. The dominant peak at 532.35 eV can therefore be ascribed to oxygen in silicates, Si–O bonds.[35,36] The

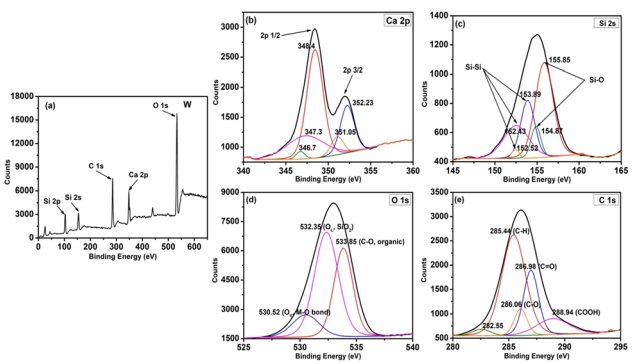

Fig. 1 XPS data for pristine wollastonite ($CaSiO_3$), including (a) full survey and (b–e) high-resolution images of individual components.

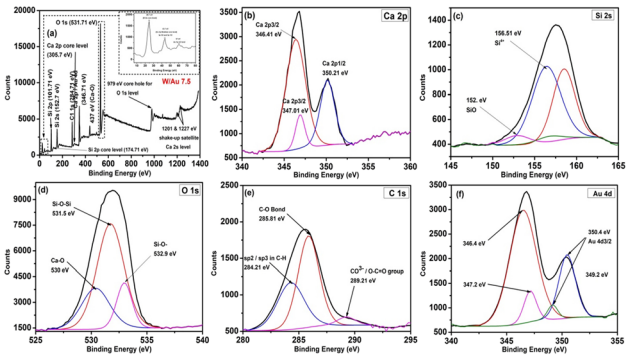

Fig. 2 XPS data for gold-doped wollastonite ($CaSiO_3$/Au) nanohybrids including, (a) full survey and (b–f) high-resolution images of individual components.

shoulder peak at 533.65 eV can be assigned to C–O bonds from organic contamination; the peak at 530.52 eV represents metal–oxygen bonds, possibly Ca–O in this case.[34,37]

Finally, Fig. 1e shows the XPS C 1s spectrum, which shows carbon species. The major peak at 285.44 eV is contributed by C–H bonds, representative of hydrocarbon contamination. The other peaks appearing at 286.98 eV (C=O), 286.06 eV (C–O), and 288.94 eV (COOH) correspond to other oxidized carbon species on the surface. The current XPS analysis confirmed the composition of the $CaSiO_3$ sample, while it also showed contamination of the surface by carbon-containing species, which is rather common for samples analyzed by XPS after atmospheric exposure.[38–40] The presence of the Si–Si bonds shows that silicon is in a somewhat more complex environment than expected, due either to surface defects or partial reduction.[35]

However, in the case of gold-doped wollastonite (W/Au) nanohybrids with a ratio of 7.5 wt/v% Au-NPs. The XPS spectrum is illustrated in Fig. 2. It can be seen from the survey spectrum in Fig. 2a that the elemental composition shows peaks at O 1s, Ca 2p, Si 2p, Si 2s, C 1s, and Au 4f. Shake-up satellite peaks are present at 1201 and 1227 eV; these correspond to electronic relaxation processes. The inset shows an expanded view of the Au 4f region, showing the occurrence of gold in the sample.[41] Fig. 2b displays the high-resolution Ca 2p spectrum; it presents a characteristic doublet with Ca 2p3/2 at 346.41 and Ca 2p1/2 at 350.21 eV. Spin–orbit splitting with peak intensities is consistent with calcium in an oxide environment.[32–34] The Si 2s spectrum in Fig. 2c is deconvoluted into two key features: a dominant peak at 156.61 eV bound to Si^{4+} in the silicate structure, and a minor peak at 152 eV for SiO, thus supporting the presence of some reduced silicon species.[42,43] Fig. 2d shows the fitted O 1s spectrum with three components: the main peak at 531.5 eV is typical for Si–O–Si bonds in the silicate network.[44] The peak at 532.9 eV corresponds to Si–O bonds,[35,36] whereas the lower binding energy peak at 530 eV is attributed to Ca–O bonds.[34,37] The C 1s spectrum (Fig. 2e) shows the carbon contaminants on the surface, with three well-separated peaks due to the C–H bonds at 284.21 eV, C–O bonds at 285.81 eV, and a higher binding energy

peak at 289.21 eV corresponding to CO_3^{2-} or O–C=O groups.[38–40] Fig. 2f shows the Au 4d spectrum, further confirming the presence of gold by the characteristic Au 4d5/2 and Au 4d3/2 peaks at 346.4 and 350.4 eV, respectively, signifying that Au-NPs or a thin layer of gold is deposited on the surface of $CaSiO_3$.[41]

3.2. Mechanical properties of gold-doped wollastonite hybrid nanocomposites

The pure wollastonite (W), represented by the black line, shows a maximum force of about 800 N before failure. The addition of Au-NPs significantly altered the mechanical properties. Doping with 1.25 wt/v% Au-NPs (depicted by the red curve) show a decrease in peak force to about 600 N, suggesting that at low concentrations, gold introduces defects or weakens the framework of the material. In contrast, as the gold concentration rises, there is a significant improvement in the attained mechanical properties.[45] Doping with 2.5 wt/v% Au-NPs (green curve) resulted in a higher maximum force of about 1000 N, exceeding that of pure wollastonite. This trend continues with 5% Au-NPs (blue curve) reaching approximately 1150 N, and doping with 7.5 wt/wt% Au-NPs (pink curve) achieving the highest force of approximately 1300 N.[46,47] Notably, the expanded curves beyond 0.8 mm before failure show improved ductility in specimens with higher gold contents (*i.e.*, 5 and 7.5 wt/v%, respectively). This implies that the inclusion of gold improves the material's strength as well as its capacity to bend plastically before breaking.[35,36] The clear trend in the curves is further supported by the Table in the inset of Fig. 3, which offers precise measurements of the ultimate force and ultimate stress. A notable improvement in mechanical strength is indicated by the peak stress, which rises dramatically from 7.15 MPa for pure $CaSiO_3$ to 11.56 MPa for the 7.5 wt/v% Au-NPs.

3.3. *In-vitro* biomineralization

The surface biomineralization images and concomitant elemental spectra for W and W/Au hybrid nanocomposites are displayed in Fig. 4 and 5, respectively, before and after immersion in simulated body fluid (SBF) at two different time points (two and four weeks, respectively). Before immersion, the images exposed that the surface appeared quasi-porous in addition to being rough and unevenly shaped. A bigger porous structure evolved when the gold content in the wollastonite phase grew by 1.25, 2.5, and 5 wt/v%, as shown in Fig. 4a–d, respectively.[3] However, in the case of W/Au 7.5 wt/v%, an uneven surface shape with a low-porous surface is obtained. This is because Au-NPs are deposited onto the wollastonite surface, as illustrated in Fig. 4e. All surfaces of the examined samples developed a self-assembled apatite layer upon immersion in simulated body fluid (SBF). This demonstrates the high *in vitro* bioactivity of the studied materials. Nevertheless, as the Au-NP concentration increased, there were variations in the layer morphology; the spherical entities that were agglomerated had larger diameters when the samples had Au-NPs. When gold was added to the sample's composition, the average pore width decreased and SSA significantly increased.[48,49] There are multiple processes involved in the apatite layer production mechanism, as follows; (a) using H^+ to exchange calcium ions; (b) surface silanol (Si–O–H) synthesis; (c) silanol group polymerization to produce amorphous silica; and (d) migration of calcium and phosphate ions and precipitation on the sample surface and apatite crystallization.[50]

Differences in dynamics with changing concentration of gold and immersion time were observed. In comparison with pure wollastonite, samples doped with 2.5 or 5 wt/v% Au-NPs showed superior bioactive characteristics, revealing more sophisticated mechanisms for surface transformation. While the samples were initially characterized by relatively smooth and porous surfaces, significant morphological changes were observed, and Ca/P ratios evolved from highly variable ranges at 2 weeks (*i.e.*, 2.09–4.82) as shown in Fig. 5f–j, to more physiologically consistent levels at 4 weeks (1.84–1.89) as shown in Fig. 5k–o, closer to the composition of natural bone apatite. In contrast, although higher concentrations of Au-NPs (*i.e.*, 7.5 wt/v%) delayed early apatite formation, the 2.5 and 5 wt/v% Au-NP-doped samples showed improved nucleation rates and surface coverage to reach a more homogeneous mineralized structure. EDX elemental distribution analysis revealed the O, P, Ca, Si, and Au-NPs. In this analysis, Au-NP nanoparticles were integrated into the structure of wollastonite. From EDX, the Ca/P ratios evolved from highly variable ranges at 2 weeks (2.45–4.84) that confirms the CaO phase began to act in the HA phase as pointed out by Mohamed *et al.*, 2014[54] to more physiologically consistent levels at4 weeks (1.67–1.843), closer to the composition of natural bone apatite (see Fig. 5). At 4 weeks, the Ca/P ratio of Au-NPs/wollastonite increased with an increase in the Au-NP concentration up to (5 and 7.5) % Au-NPs-doped wollastonite reached 1.843, compared with pure wollastonite (W) ~1.76 and 1.25, 2.5 wt/v% Au-NPs-doped wollastonite (W/Au) ~1.69, such values were higher than the stoichiometric value of HA ~1.67, thus displaying the formation of carbonated hydroxyapatite (CHA) of the B-type, which resembles real bone apatite of poor crystallinity. All samples were characterized by an increase in oxygen content to 40–50%, stabilization of calcium at 25–35%, phosphorus increasing to 10–15%, and a systematic decrease in silicon content, indicating intensive

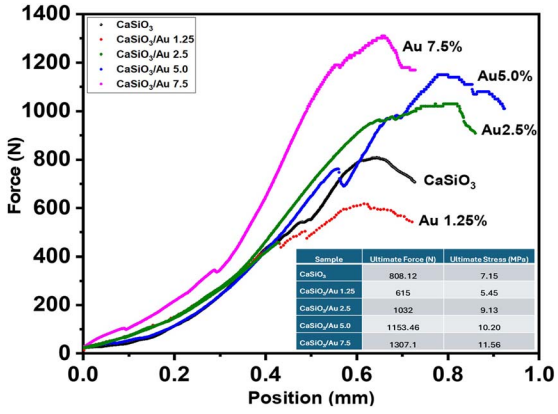

Fig. 3 Compressive strength values of wollastonite (W) and gold-doped wollastonite (W/Au) with different ratios of Au-NPs.

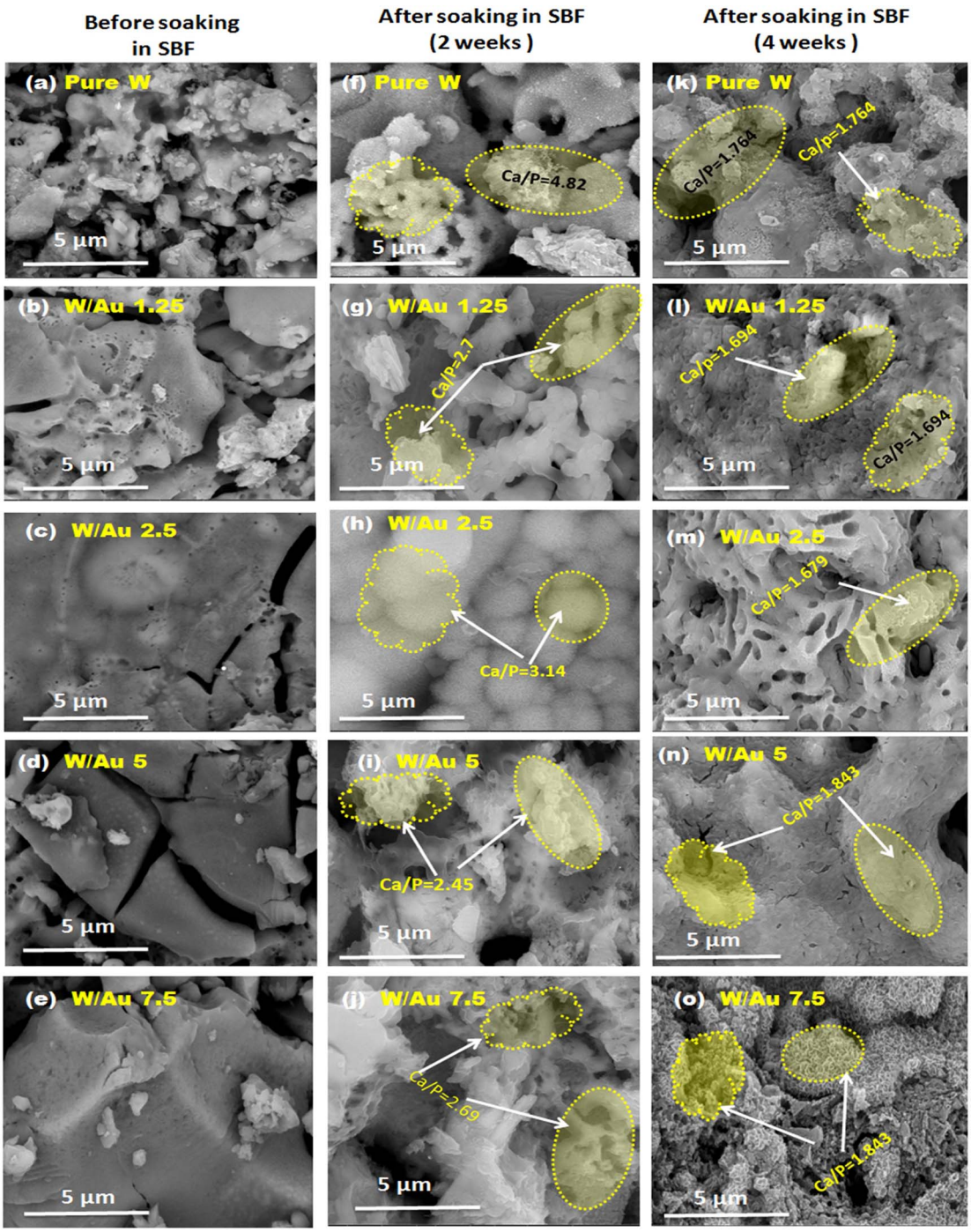

Fig. 4 SEM micrographs before soaking in SBF of pure wollastonite (W) and gold-doped wollastonite nanohybrids (W/Au) samples (treated at 1200 °C per 2 h) (a–e) and after immersion in SBF for 2 weeks (f–j) and for 1 month (k–o).

surface metamorphosis. Meanwhile, the 4-weeks immersion showed remarkable improvement in biomimetic properties compared to the 2-weeks interval, with larger apatite crystals that have a fully developed morphology, more even elemental distribution, and more complete integration of the mineralized layer. These observations not only emphasize the influence of gold doping on regulating the bioactive properties of wollastonite (W) but also perhaps provide a quantitative basis by which biomaterial design in applications related to bone tissue can be optimized.[51,52]

3.4. Biodegradation, pH evaluation and ion release

3.4.1. Biodegradation and pH evaluation. The weight loss and erosion behavior (%), water absorption (swelling), and pH values variations 'analysis of wollastonite and gold-doped wollastonite hybrid nanocomposites over a one-month

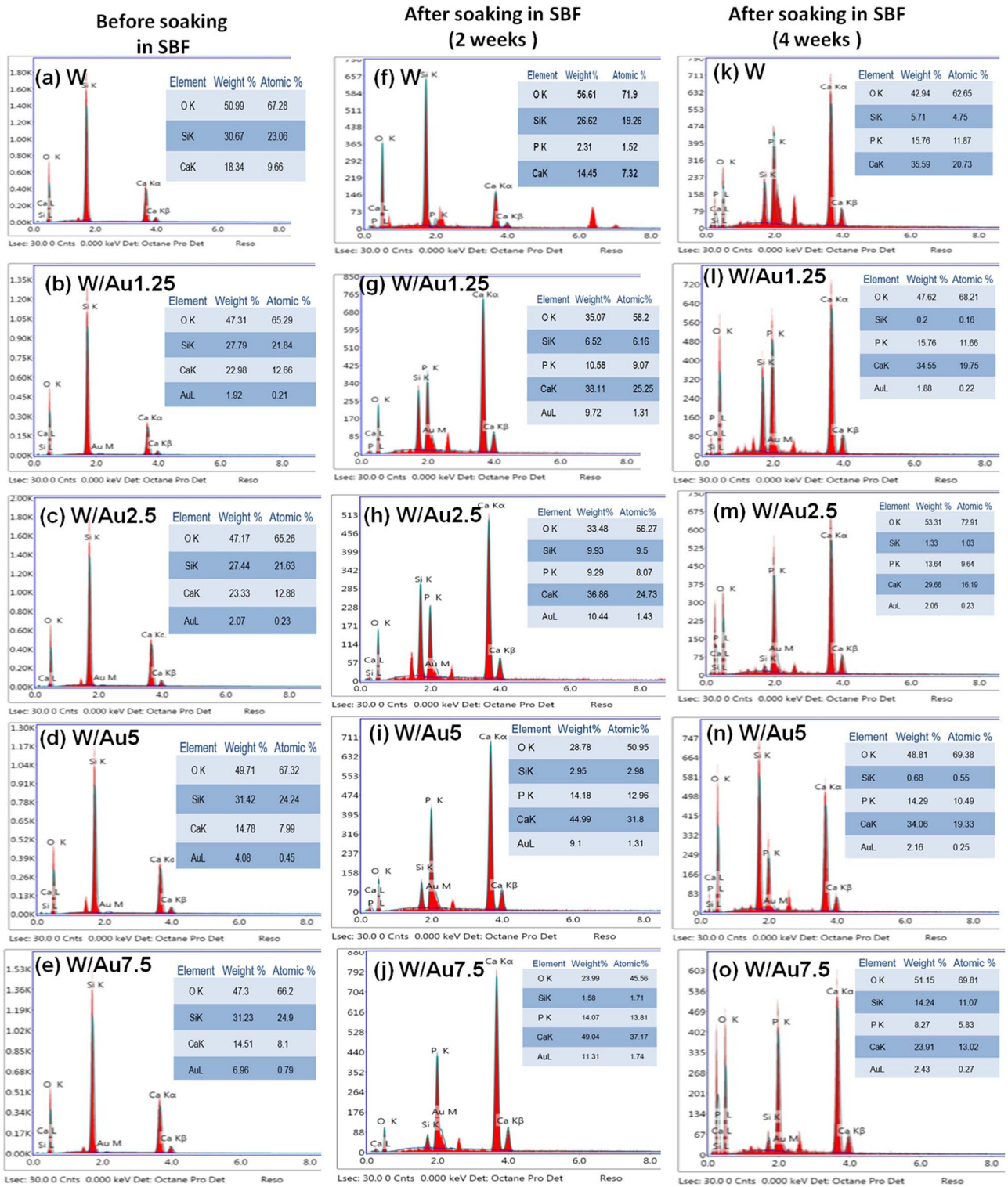

Fig. 5 EDX of pure wollastonite (W) and gold-doped wollastonite nanohybrids (W/Au-NP) samples (treated at 1200 °C per 2 h) before (a–e) and after soaking in SBF for 2 weeks (f–j) and for 1 month (k–o).

immersion in SBF are illustrated in Fig. 6, showing certain key interconnected relationships. In the case of weight loss, all samples from W to W/Au7.5 wt/v% showed an increasing trend of weight loss with time. In general, the two higher-concentration compositions, W/Au 5 and W/Au 7.5 wt/v%, showed higher weight loss compared to the rest of the samples. On day 30, all samples exhibited weight loss of approximately 12–16%. The rate of weight loss was steeper in the first 15 days and then decreased. In the case of water absorption, all samples exhibited values between 60% and 85%. Composition of W/Au 5

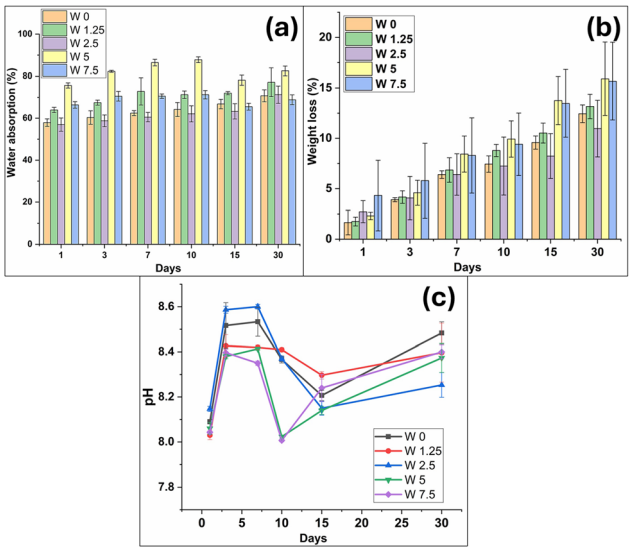

Fig. 6 (a) Water adsorption, (b) weight loss and (c) pH value after immersion of nanoparticles in SBF at different time intervals.

wt/v% showed high stability for water absorption, amounting to about 80–85%. The lowest mixtures, such as W and W1.25 wt/v%, gave relatively stable but lower levels of water absorption. Water absorption was initially rapid in the first couple of days, followed by stabilization. The pH changes over time exhibited a distinct trend. The pH of all samples increased rapidly from day 0 to day 5, reaching values around 8.4–8.6. However, the pH then significantly decreased around day 10 and stabilized by day 30 between 8.2-8.4. Interestingly, the W2.5 wt/v% composition exhibited the largest initial pH spike, reaching approximately 8.6.

These relationships between weight loss, water absorption, and pH changes reflect a complex interplay among material degradation, hydration, and the chemical environment. Higher water absorption is generally correlated with greater weight loss, indicating that the degradation mechanism is linked to water uptake.

The initial increase in pH coincided with the period of rapid water uptake, and the changing pH could influence the degradation rate and hence the weight loss. From day 15 onwards, the rate of weight loss decreased as the pH stabilized. In the overall context, W/Au 5 wt/v% composition appears to represent an optimum compromise among the important parameters, showing controlled weight loss, high water absorption, and a stable pH profile, all significant parameters of biomaterial performance in tissue engineering. From the earlier results, it was concluded that all samples exhibited mild and controlled deterioration (12–16%) throughout the immersion duration, and the pH test revealed that the pH remained within the physiological range. Improved swelling that maintains structural integrity while demonstrating improved cellular interaction.

3.4.2. Ion release. The formation of calcium phosphate depositions on the external surfaces of the sample discs can be indirectly demonstrated by the change in the amount of Ca and P ions in the SBF solution.[26,56] The concentrations of Ca^{2+} (ppm) and phosphate (ppm) ions released into the SBF solution at certain times are shown in Fig. 7. The release profiles of the two ions displayed a similar pattern with zigzag behavior over time.

At the beginning of immersion, the calcium ion concentration starts around 205 ppm for the pure wollastonite (W) and decreases over time. When the gold doping concentration increased (*i.e.*, W/Au 1.25 to W/Au 7.5 wt/v%), the initial calcium ion concentration and the rate of decrease over time both became lower. The phosphate ion concentration initially increased for (W/Au 7.5 wt/v%) compared with pure (W), peaking around day 15 for (W/Au 2.5 wt/v%) and then decreasing over time. The silica ion concentration steadily increased over time for all compositions, but in general, their concentration was not high, which may be attributed to the low and steady degradation of our samples and at the end of immersion time, due to apatite layer coverage that may hinder the silica ion release. The Au-NPs release was highest for the highest concentration of gold nanoparticles doping (W/Au 7.5 wt/v%) compared to other gold-doped samples.

As shown in Fig. 7, the 0.1 ppm Au^{3+} ion release rate for local bone implantation was within the safe ranges for human use and far below the toxicity levels reported in the literature. Experiments involving gold nanoparticles and gold coatings for medical devices typically indicate that issues arise at much greater concentrations. By comparison with the literature, 0.1 ppm appears to be within the safe range for bone implant applications. Experiments have established higher toxicity levels: aquatic life is cytotoxic at 0.62–2 ppm (LC_{50} at 48 h)[53–55] and 14.4 ppm (at 96 h),[53] and broiler chickens have been reported to be damaged by 15 ppm exposure.[55,56] The 0.1 ppm release can be described as subacute compared with the reported acute toxicity levels.

Yet, caution is required as particle size dictates toxicity (smaller particles <10 nm with greater biodistribution), surface characteristics dictate cytotoxicity (citrate-coated particles being more toxic than starch or gum Arabic-coated counterparts), and long-term effects can arise from gold nanoparticles' tendency to

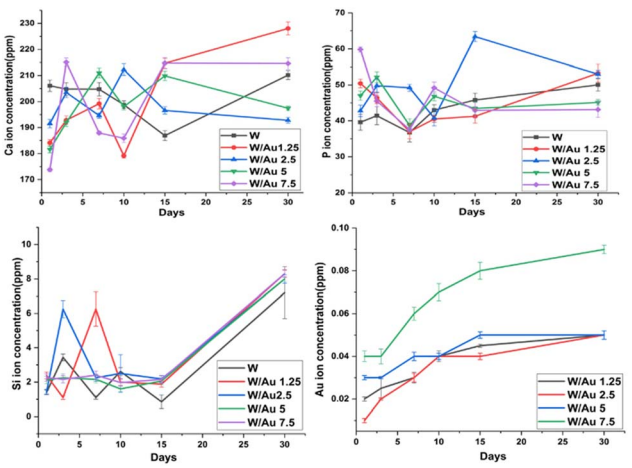

Fig. 7 Calcium, phosphorus, silica and gold ions released from prepared nanoparticles after immersion in SBF.

accumulate in certain organs, predominantly the liver and spleen.[57] Although acute toxicity at 0.1 ppm appears to be low for bone implant applications, bioaccumulation and chronic effects cannot be eliminated, given the persistence of gold nanoparticles in the biological system.

3.5. *In vivo* studies

3.5.1. Impact of Au-NP doping on Bmp-2, Runx2, and SMAD1. After one and two months, the bone defects caused a reduction in Bmp-2 by 77% and 71% and in Runx2 bone content by 84% and 71%, respectively, compared with normal rats. The implantation with Au-NPs 1.25, 2.5, 5, 7.5 mg kg^{-1} elevated the levels of the osteogenic markers Bmp2 after 1 month by 55%, 123%, 153% and 189%, and after 2 months by 102%, 139%, 179% and 226%, and increased Runx2 after 1 month by 100%, 194%, 241% and 315%, and after 2 months by 132%, 168%, 213% and 237%, compared with the positive control. In addition, Au-NPs 7.5 wt/v% implantation increased Bmp2 after 1 and 2 months by 91% and 58%, respectively, and Runx2 bone content after 1 and 2 months by 105% and 49%, respectively, compared with the drug and returned to normal levels after 2 months (see Fig. 8).

Bone defects reduced Smad 1 bone content after 1 and 2 months by 86% and 73%, respectively, compared with normal rats, whereas Au-NPs implantation at 1.25, 2.5, 5, 7.5 mg kg^{-1} up-regulated the level of Smad after 1 month by 213%, 333%, 406% and 485% and 2 months by 96%, 140%, 197% and 278% compared with the positive control. In addition, Au-NPs 7.5 wt/v% implantation increased Smad 1 bone content after 1 and 2 months by 86% and 85%, respectively, compared with the drug and returned it to normal level after 2 months (Fig. 8). Data were presented as mean ± standard deviation (S.D.) and estimated by one-way analysis of variance (ANOVA) followed by Fisher's LSD post-hoc test. The same letter indicates a non-significant difference, whereas different letters indicate a significant difference at $p < 0.05$.

3.5.2. Effect of Au-NPs doping on GSK3β and alkaline phosphatase. GSK3β was elevated with bone defect by15-fold after 1 month and 11-fold after 2 months, respectively, compared with normal rats, whereas Au-NPs 1.25, 2.5, 5, 7.5 mg kg^{-1} implantation reduced GSK3β elevations after 1 month by 24%, 49%, 64% and 79%, respectively, and 2 months by 32%, 66%, 80% and 95%, respectively, compared with the positive control. In addition, Au-NPs 7.5 wt/v% implantation reduced GSK3β bone content after 1 and 2 months by 70% and 94%, respectively, compared with the drug, and returned it to a normal level after 2 months (Fig. 9).

Alkaline phosphatase was reduced with bone defects by 83% after 1 month and 82% after 2 months, respectively, compared with normal rats, whereas Au-NPs 1.25, 2.5, 5, 7.5 mg kg^{-1} implantation elevated alkaline phosphatase elevations after 1 month by 128%, 203%, 283% and 283%, and 2 months by 133%, 219%, 317% and 327%, compared with the positive control. In addition, W/Au 7.5 wt/v% implantation elevated alkaline phosphatase serum levels after 1 and 2 months by 155% and 164%, respectively, compared with pure wollastonite and returned to normal levels after 2 months (Fig. 9).

Data were presented as mean ± standard deviation (S.D.) and evaluated by one-way analysis of variance (ANOVA) followed by Fisher's LSD post-hoc test. The same letter indicates a non-significant difference, while different letters indicate a significant difference at $p < 0.05$.

Osteoblast activity coordinates bone growth as part of the defensive mechanism against bone loss. Osteoblasts produce Bmp2, a transforming growth factor-beta.[58] It plays a vital role in osteogenesis and bone growth[59] by modulating Runx2 expression, which is in turn involved in osteoblast differentiation.[60] wollastonite (W) and gold-doped wollastonite (W/Au) nanohybrids, especially high-ratio doping, elevated Bmp2 and Runx2 bone contents. It is suggested in this study that Au-NPs doping

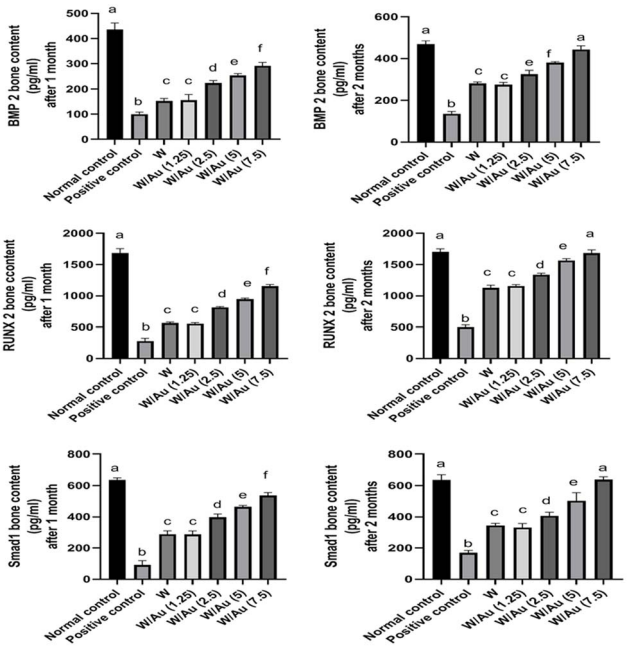

Fig. 8 Effect of Au-NPs on Bmp-2, Runx2 and Smad1.

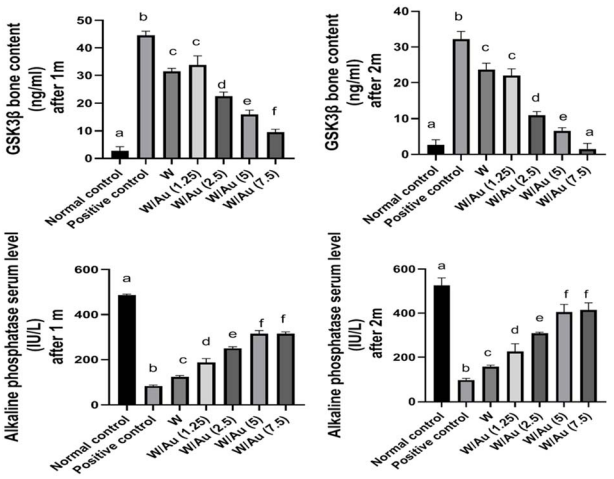

Fig. 9 Effect of Au-NPs on GSK3β and alkaline phosphatase.

showed improvement of bone mass *via* Bmp2 and Runx2 up-regulation. Previously, Au-NPs-loaded mesoporous silica nanoparticles promoted osteogenic activity by regulating the immune microenvironment.[13] The presence of silica inhibits the formation of osteoclast-like cells and promotes osteogenic differentiation.[61]

Smad 1 protein regulates BMP signal transduction and the transcription of osteogenic-related genes that promote bone formation.[62] In this study, Au-NPs doping increased Smad 1 bone content compared with the positive control. In another study, bioactive glass doped with Au-NPs nanoparticles had a proliferative impact on the human bone cell line.[63] Gold nanostructures have a therapeutic effect on cartilage tissue and chondrocytes.[64]

Glycogen synthase kinase-3 (GSK3) is a kinase found in most cells that contributes to multiple signaling pathways (predominantly post-translational modifications, cellular trafficking, substrate priming, and protein complexes). It has two GSK3 isoforms, GSK3α and GSK3β, which are involved in the etiology and treatment of several disorders, including inflammatory diseases, psychiatric and neurological diseases, cancer, and others.[65] Inhibition of glycogen synthase kinase-3β inhibits inflammatory reactions and stimulates osteogenesis induction and bone regeneration.[66] Our results revealed that Au-NP doping reduced GSK 3β bone content compared with the positive control, thereby suppressing inflammation. At the same time, Au-NP increased serum alkaline phosphatase level, which is a representative bone metabolism marker.[67] Furthermore, GSK-3 inhibition enhanced mineral nodule formation by cement oblasts and regulated crucial differentiation markers of cement oblasts, such as Alp, Runx-2 and Osteocalcin.[64] However, the findings illustrated that Au-NPs suppress GSK-3, which stimulates cement oblasts to form nodules, by raising ALP and Runx-2 levels in bone. This suggests that Au-NP doped composites can be a promising alternative for bone defect repair.

3.5.3. Bone mineral density (BMD). Bone mineral density of the grafted defect area with different materials in addition to the positive control and normal control groups was measured at 1- and 2-months post-surgery and the findings are illustrated in Table 2 and Fig. 10, respectively. All grafted and positive control groups showed increased bone mineral density over the grafting period, as the data makes evident. BMD increase is due to bone maturation and mineralization over time. As the percentage of gold in the samples increased, there was a corresponding increase in bone density. After one or two months, the bone density of the samples with higher concentrations of gold (Au-NPs 2.5, Au-NPs 5, and Au-NPs 7.5) was almost identical to that of the control. This behavior may be ascribed to Au-NPs, which stimulate osteoblast progression and suppress osteoclast differentiation, as indicated elsewhere.[45] Another similar study showed that the administration of gold nanoparticles enhances bone mineral content markers and decreases bone resorption markers of serum levels.[68]

3.5.4. Histopathological investigation. The rat groups maintained as controls showed normal histological structure and no histopathological changes were recorded after one or two months (Fig. 11a and b). Group of rats (blank): there was a focal damaged area after one or two months (Fig. 11c and d). Group of rats (pure W): newly formed osteoblasts were detected at the periphery of the bone with intact osteocytes and dilated blood capillaries after one month and there was a wide area of intact osteocytes after two months (Fig. 11e and f). Group of rats (W/Au1.25 wt/v%): Focal areas of newly formed blood capillaries and osteoblasts were observed after one month and there was a diffuse intact area of osteocytes after two months (Fig. 11g and h). Group of rats (W/Au2.5 wt/v%): There was a condensed area of osteocytes and dilated blood capillaries after one month and a wide area of intact osteocytes was detected after two months (Fig. 11i and j). Group of rats (W/Au5 wt/v%): there were newly formed blood capillaries, and they were surrounded by intact osteocytes after one month and a diffuse area of intact osteocytes with dilated blood capillaries was detected after two months (Fig. 11k and l). Group of rats (W/Au7.5 wt/v%): diffuse intact osteocytes were observed after one month and there was a diffused area of intact osteocytes after two months (Fig. 11m and n).

Table 2 Bone mineral density measurements at one- and two-months post-surgery for different groups[a]

	BMD	
Group name	1 Month	2 Months
Control (healthy bone)	0.263 ± 0.014	0.263 ± 0.014
Positive control (empty defects)	0.131 ± 0.007	0.151 ± 0.008
W	0.192 ± 0.009	0.234 ± 0.012
W/Au 1.25	0.206 ± 0.010	0.258 ± 0.013
W/Au 2.5	0.249 ± 0.12	0.278 ± 0.013
W/Au 5	0.250 ± 0.013	0.292 ± 0.015
W/Au 7.5	0.290 ± 0.015	0.298 ± 0.024

[a] Data were presented as mean ± standard deviation (S.D.) and evaluated by one-way analysis of variance (ANOVA) followed by Fisher's LSD post-hoc test. The same letter indicates a non-significant difference, whereas different letters indicate a significant difference at $p < 0.05$.

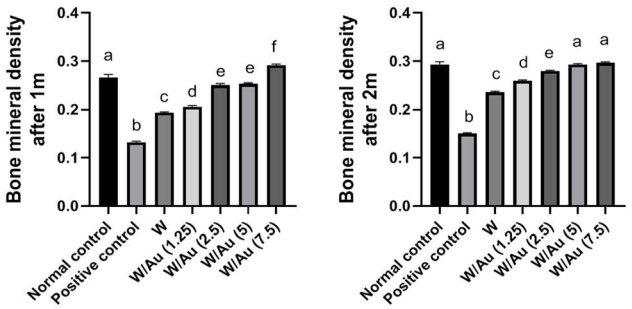

Fig. 10 Effect of Au-NPs on bone mineral density.

3.6. Benchmarking commonly used bone grafted materials

Studies of wollastonite (W/Au) nanohybrids doped with gold reveal a range of benefits, positioning the material, as mentioned earlier, at the same level as conventional

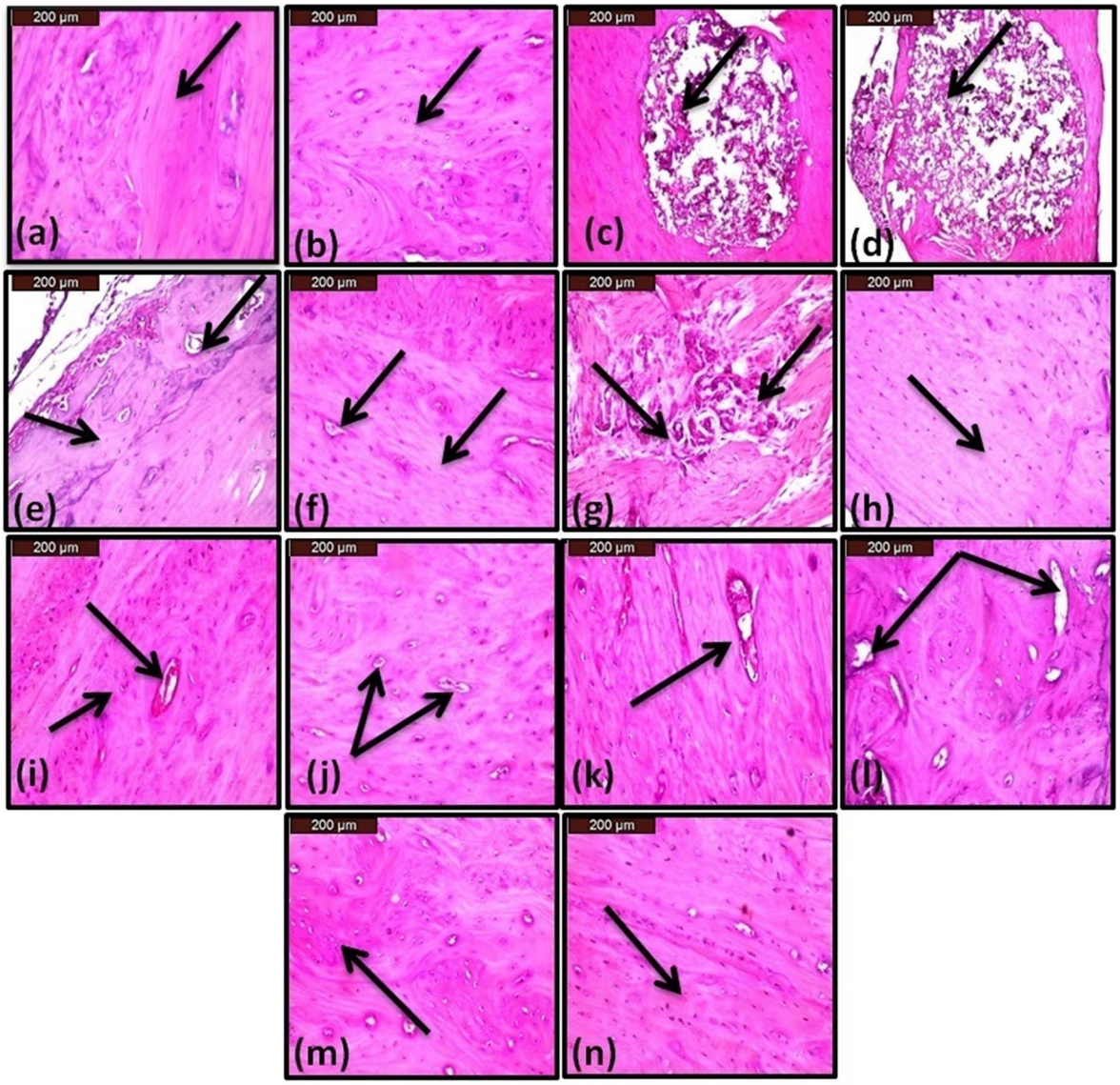

Fig. 11 Effect of Au-NPs on bone histopathology, normal control after 1 and 2 months (a and b) with black arrows indicating normal osteoblasts, positive control after 1 and 2 months (c and d) with black arrows indicating perforation, drug after 1 and 2 months (e and f) with black arrows indicating osteoblasts and blood vessels(BVs), Au-NP 1.25 after 1 and 2 months (g and h) with black arrows refer to g) newly formed capillaries and (h) normal osteoblasts, Au-NP 2.5 after 1 and 2 months (i and j) with black arrows indicating normal osteoblasts, Au-NP 5 after 1 and 2 months (k and l) with black arrows refer to normal osteoblasts, Au-NP7.5 after 1 and 2 months (m and n) with black arrows indicating normal bone.

biomaterials such as hydroxyapatite (HA) and bio-glass in bone tissue engineering.[21]

Gold-doped wollastonite nanohybrids exhibit significantly enhanced mechanical properties relative to low mechanical strength and low biodegradation rates for conventional hydroxyapatite.[10,22] This represents a significant advance over HA, which tends to require composite formulations that possess adequate mechanical properties for load-bearing applications.[69,70] The wet chemical synthesis technique used for W/Au offers better compositional control than the high-temperature processing typically required for dense HA.[3,71,72] While bio-glass shows good bioactivity through rapid ion exchange, the W/Au nanohybrids showed controlled and stable biodegradation with improved swellability (80–85% for W/Au 5 wt%/v.%), which can be utilized for improved vascularization and cell infiltration. It has a more controlled degradation profile than certain bio-glass formulations that tend to degrade too rapidly in physiological environments.[63,73,74]

The *in vivo* tests revealed that the W/Au nanohybrids stimulated the BMP2/Smads1/Runx2 pathway necessary for osteoblast differentiation, the same as bioactive glasses, but with the added effect of gold nanoparticles inhibiting GSK-3β, also stimulating osteogenesis. This dual mechanism of action is distinct from that of traditional hydroxyapatite, which primarily provides an osteoconductive scaffold without any inherent signalling enhancement property.[10,13,20]

The elevated alkaline phosphatase activity and enhanced bone mineral density two months after implantation, together

with histopathology evidence of proliferation of blood vessels and osteoblasts, reveal that W/Au nanohybrids can render improved integration properties compared to traditional hydroxyapatite scaffolds, which tend to show delayed integration and remodeling.[75,76]

Furthermore, the ability to tune the gold content (0–7.5 wt%/v.%) in such nanohybrids enables a programmable scaffold to improve biological and mechanical properties compared to traditional bio-glass and hydroxyapatite systems with limited compositional flexibility.[12,22]

4. Conclusion

This work presents, for the first time, strong evidence to prove that gold-doped Wollastonite nanohybrids may serve as a revolutionary biomaterial for bone regeneration. The systematic synthesis and characterization showed that the incorporation of Au-NPs into Wollastonite significantly improved not only its mechanical properties but also its biological performance. The nanohybrids exhibit a well-balanced combination of biocompatibility, biodegradability, and bioactivity, making them suitable for orthopedic and bone tissue engineering applications.

In vitro tests confirmed that W/Au nanohybrids significantly facilitate the deposition of apatite layers after biomineralization in SBF. The highest degree of bioactivity, in terms of this study, was recorded for W/Au 5 wt/v% material. Besides the structural stability of this material, the achievement of controllable biodegradation and good water absorption suggests that it provides a conducive microenvironment for cell activities. The results were further corroborated in *in vivo* experiments using a rat femur defect model in which W/Au nanohybrids effectively promoted the expression of major osteogenic markers, such as bone morphogenetic protein 2, Smads1, and Runx2, through the BMP2/Smads1/Runx2 signaling pathway. Attenuation of inflammatory markers, such as glycogen synthase kinase-3β, coupled with increased alkaline phosphatase activity, demonstrated the dual role of W/Au nanohybrids in activating osteogenesis while modulating inflammation, which was considered the first reported study.

Histopathological analysis showed not only improvement in osteoblast proliferation and angiogenesis and a general improvement in bone quality. Mechanical tests revealed that gold doping reinforced the material, where the highest compressive strength was 11.56 MPa for W/Au 7.5 wt/v%, while pure wollastonite had a value of 7.15 MPa. However, W/Au 5 wt/v% was found to be the optimal composition because it provided the best balance between mechanical performance and bioactivity. Bone mineral density measurements showed that all W/Au nanohybrids favored bone maturation and mineralization. Results were close to those for healthy bones. These findings highlight the multi-functional advantages of W/Au nanohybrids, which are a promising alternative to traditional bone grafts and implants. Modulation of cellular signaling pathways, promotion of osteogenic differentiation, and enhancement of mechanical integrity are potential candidates for clinical application in treating bone defects caused by trauma, disease, or surgical interventions. The stability and biocompatibility of the W/Au nanohybrids should be deeply explored in various physiological media, as well as performance in larger animal models by scaling up optimization. Moreover, this study can help us comprehend the function of the immunomodulatory effects of Au-NPs during the process of bone regeneration and healing.

Consent to publications

All authors accepted the publication of the manuscript in the present form.

Ethical approval

This study was conducted in compliance with the Federal Wide Assurance (FWA) 00014747 and RHDIRB: 2017103002 guidelines, ethics regulations issued by the Egyptian Drug Authority (EDA) and the Minister of Health & Population, Cairo, Egypt. The study was approved by the Medical Research Ethics Committee on June 02, 2023, with approval number 02540223.

Data availability

The authors confirm that the data supporting the findings of this study are available within the article.

Author contributions

Mona Moaness: contributed to the conceptualization and planning of the study; performed *in vitro* bioactivity assay, SEM-EDS investigation, biodegradation, and ion release measurements for wollastonite doped with AuNPs; and contributed to the histopathological data analysis for wollastonite doped with AuNPs. Data analysis, formulation, and revision. Ahmed Nabile Emam: conceptualization of the study as a Co-PI for NRC in-house grant (ID: 13020224), preparation of gold nanoparticles (AuNPs), conducted X-ray photoelectron spectroscopy (XPS) characterization experiments. He also contributed to data analysis, formulating and revising the manuscript through final submission and acceptance. Abeer Salama: Performed biochemical markers analysis and performed the statistical analysis for whole data. Manar M. Ahmed: Performed *in vitro* bioactivity, ion release, biodegradation and SEM-EDS investigations for wollastonite doped with AuNPs. E. M. A. Hamzawy: contributed to the idea and design of the research, prepared wollastonite doped with AuNPs, and revision of the manuscript. Areg E Omar: *in vivo* experiments, collecting biological samples, animal surgical procedures, and contribute into bone mineral density measurements. Gehan T. El-Bassyouni: Project PI and contributed to planning and conceptualizing this study through an NRC in-house grant (ID: 13020224). In addition, contributed to the preparation of the wollastonite doped with gold nanoparticles (AuNPs) and revised the manuscript.

Conflicts of interest

There are no conflicts to declare.

Acknowledgements

The authors would like to thank the National Research Centre (NRC) for providing financial support through their in-house grant (ID: 13020224). This grant, titled "Bioactivity of Au-NPs containing wollastonite through *in vitro* and *in vivo* tests and their cytotoxicity," is led by Principal Investigator Prof. Gehan T. El-Bassyouni.

References

1 N. Xue, X. Ding, R. Huang, R. Jiang, H. Huang, X. Pan, W. Min, J. Chen, J.-A. Duan, P. Liu and Y. Wang, Bone tissue engineering in the treatment of bone defects, *Pharmaceuticals*, 2022, **15**(7), 879.

2 J. W. Łuczak, M. Palusińska, D. Matak, D. Pietrzak, P. Nakielski, S. Lewicki, M. Grodzik and Ł. Szymański, The future of bone repair: emerging technologies and biomaterials in bone regeneration, *Int. J. Mol. Sci.*, 2024, **25**(23), 12766.

3 A. N. Emam, M. N. Ahmed, G. T. El-Bassyouni, E. M. A. Hamzawy and M. Moaness, Gold doped wollastonite hybrid nanocomposites as a candidate for bone regeneration/healing applications: biocompatibility and antimicrobial efficacy, *Ceram. Int.*, 2024, **50**(14), 26000–26017.

4 S. S. Eldera, N. Alsenany, S. Aldawsari, G. T. El-Bassyouni and E. M. A. Hamzawy, Characterization, biocompatibility and *in vivo* of nominal MnO_2-containing wollastonite glass-ceramic, *Nanotechnol. Rev.*, 2022, **11**(1), 2800–2813.

5 S. K. Taha, M. A. Abdel Hamid, E. M. A. Hamzawy, S. H. Kenawy, G. T. El-Bassyouni, E. A. Hassan and H. E. Tarek, Osteogenic potential of calcium silicate-doped iron oxide nanoparticles *versus* calcium silicate for reconstruction of critical-sized mandibular defects: an experimental study in dog model, *Saudi Dent. J.*, 2022, **34**(6), 485–493.

6 M. Mabrouk, S. K. Taha, M. A. Abdel-Hamid, S. H. Kenawy, E. A. Hassan and G. T. El-Bassyouni, Radiological evaluations of low cost wollastonite nanoceramics graft doped with iron oxide in the treatment of induced defects in canine mandible, *J. Biomed. Mater. Res., Part B*, 2021, **109**(7), 1029–1044.

7 M. Zaidi, T. Yuen, L. Sun and C. J. Rosen, Regulation of skeletal homeostasis, *Endocr. Rev.*, 2018, **39**(5), 701–718.

8 G. Bheemaneni, S. Saravana and R. Kandaswamy, Processing and characterization of poly (butylene adipate-co-terephthalate)/wollastonite biocomposites for medical applications, *Mater. Today: Proc.*, 2018, **5**(1), 1807–1816.

9 M. Y. Shie, S. J. Ding and H. C. Chang, The role of silicon in osteoblast-like cell proliferation and apoptosis, *Acta Biomater.*, 2011, **7**(6), 2604–2614.

10 Y. Huang, C. Wu, X. Zhang, J. Chang and K. Dai, Regulation of immune response by bioactive ions released from silicate bioceramics for bone regeneration, *Acta Biomater.*, 2018, **66**, 81–92.

11 N. Biswas, A. Samanta, S. Podder, C. K. Ghosh, J. Ghosh, M. Das, A. K. Mallik and A. K. Mukhopadhyay, Phase pure, high hardness, biocompatible calcium silicates with excellent anti-bacterial and biofilm inhibition efficacies for endodontic and orthopaedic applications, *J. Mech. Behav. Biomed. Mater.*, 2018, **86**, 264–283.

12 E. K. Papynov, O. O. Shichalin, V. I. Apanasevich, N. G. Plekhova, B. IYu, S. V. Zinoviev, V. Yu Mayorov, A. N. Fedorets, E. B. Merkulov, D. Kh Shlyk, V. A. Nepomnyushchaya, Z. E. Kornakova, I. S. Afonin, I. O. Evdokimov and O. V. Korshunova, Synthetic nanostructured wollastonite: composition, structure and "in vitro" biocompatibility investigation, *Ceram. Int.*, 2021, **47**(16), 22487–22496.

13 H. Liang, C. Jin, L. Ma, X. Feng, X. Deng, S. Wu, X. Liu and C. Yang, Accelerated bone regeneration by gold-nanoparticle-loaded mesoporous silica through stimulating immunomodulation, *ACS Appl. Mater. Interfaces*, 2019, **11**(44), 41758–41769.

14 G. Chen, C. Deng and Y. P. Li, TGF-β and BMP signaling in osteoblast differentiation and bone formation, *Int. J. Biol. Sci.*, 2012, **8**(2), 272–288.

15 M. Phimphilai, Z. Zhao, H. Boules, H. Roca and R. T. Franceschi, BMP signaling is required for RUNX2-dependent induction of the osteoblast phenotype, *J. Bone Miner. Res.*, 2006, **21**(4), 637–646.

16 T. M. Liu and E. H. Lee, Transcriptional regulatory cascades in Runx2-dependent bone development, *Tissue Eng., Part B*, 2013, **19**(3), 254–263.

17 M. Bruderer, R. G. Richards, M. Alini and M. J. Stoddart, Role and regulation of RUNX2 in osteogenesis, *Eur. Cells Mater.*, 2014, **28**, 269–286.

18 M. Fujii, K. Takeda, T. Imamura, H. Aoki, T. K. Sampath, S. Enomoto, M. Kawabata, M. Kato, H. Ichijo and K. Miyazono, Roles of bone morphogenetic protein type I receptors and Smad proteins in osteoblast and chondroblast differentiation, *Mol. Biol. Cell*, 1999, **10**(11), 3801–3813.

19 S. Zhu, W. Chen, A. Masson and Y. P. Li, Cell signaling and transcriptional regulation of osteoblast lineage commitment, differentiation, bone formation, and homeostasis, *Cell Discovery*, 2024, **10**(1), 71.

20 M. Dong, G. Jiao, H. Liu, W. Wu, S. Li, Q. Wang, D. Xu, X. Li, H. Liu and Y. Chen, Biological silicon stimulates collagen type 1 and osteocalcin synthesis in human osteoblast-like cells through the BMP-2/Smad/RUNX2 signaling pathway, *Biol. Trace Elem. Res.*, 2016, **173**(2), 306–315.

21 C. G. Zenebe, A review on the role of wollastonite biomaterial in bone tissue engineering, *BioMed Res. Int.*, 2022, **2022**(1), 4996530.

22 Y. J. No, J. J. Li and H. Zreiqat, Doped calcium silicate ceramics: a new class of candidates for synthetic bone substitutes, *Materials*, 2017, **10**(2), 153.

23 A. Bozorgi, M. Khazaei, M. Soleimani and Z. Jamalpoor, Application of nanoparticles in bone tissue engineering; a review on the molecular mechanisms driving osteogenesis, *Biomater. Sci.*, 2021, **9**(13), 4541–4567.

24 H. Liang, X. Xu, X. Feng, L. Ma, X. Deng, S. Wu, X. Liu and C. Yang, Gold nanoparticles-loaded hydroxyapatite composites guide osteogenic differentiation of human mesenchymal stem cells through Wnt/β-catenin signaling pathway, *Int. J. Nanomed.*, 2019, **2019**, 6151–6163.
25 D. Lee, D. N. Heo, H. J. Kim, W. K. Ko, S. J. Lee, M. Heo, J. B. Bang, J. B. Lee, D. S. Hwang, S. H. Do and I. K. Kwon, Inhibition of osteoclast differentiation and bone resorption by bisphosphonate-conjugated gold nanoparticles, *Sci. Rep.*, 2016, **6**(1), 27336.
26 T. Kokubo and H. Takadama, How useful is SBF in predicting *in vivo* bone bioactivity?, *Biomaterials*, 2006, **27**(15), 2907–2915.
27 M. Moaness, S. M. Mousa, M. T. Abo Elfadl and G. T. El-Bassyouni, Doxorubicin loaded cerium substituted hydroxyapatite nanoparticles: a promising new therapeutic approach for bone regeneration, doxorubicin delivery, and cancer treatment, *Int. Pharm.*, 2024, **654**, 123969.
28 H. S. Zayed, S. Saleh, A. E. Omar, A. K. Saleh, A. Salama and E. Tolba, Development of collagen–chitosan dressing gel functionalized with propolis–zinc oxide nanoarchitectonics to accelerate wound healing, *Int. J. Biol. Macromol.*, 2024, **261**(Pt 2), 129665.
29 H. Hao, N. Amizuka, K. Oda, N. Fujii, H. Ohnishi, A. Okada, S. Nomura and T. Maeda, A histological evaluation on self-setting α-tricalcium phosphate applied in the rat bone cavity, *Biomaterials*, 2004, **25**(3), 431–442.
30 A. E. Omar, A. M. Ibrahim, T. H. Abd El-Aziz, Z. M. Al-Rashidy and M. M. Farag, Role of alkali metal oxide type on the degradation and *in vivo* biocompatibility of soda-lime-borate bioactive glass, *J. Biomed. Mater. Res., Part B*, 2021, **109**(7), 1059–1073.
31 A. L. Mohamed, H. Elmotasem and A. A. Salama, Colchicine mesoporous silica nanoparticles/hydrogel composite loaded cotton patches as a new encapsulator system for transdermal osteoarthritis management, *Int. J. Biol. Macromol.*, 2020, **164**, 1149–1163.
32 R. E. Mostafa and A. A. Salama, Eplerenone modulates the inflammatory response in monosodium iodoacetate-induced knee osteoarthritis in rats: involvement of RANKL/OPG axis, *Life Sci.*, 2023, **316**, 121405.
33 A. A. Salama, H. A. El-Hashemy and A. B. Darwish, Formulation and optimization of lornoxicam-loaded bilosomes using 2^3 full factorial design for the management of osteoarthritis in rats: modulation of MAPK/Erk1 signaling pathway, *J. Drug Delivery Sci. Technol.*, 2022, **69**, 103175.
34 J. Abenojar, I. Colera, M. A. Martinez and F. Velasco, Study by XPS of an atmospheric plasma-torch treated glass: influence on adhesion, *J. Adhes. Sci. Technol.*, 2010, **24**(11–12), 1841–1854.
35 C. Liang, T. Lu, F. He, J. Zhang, T. Yue and J. Ye, In vitro biomineralization behaviors and mechanism as well as cell responses of calcium silicate ceramics, *J. Mater. Sci.*, 2022, **57**(31), 14655–14667.
36 Y. Y. García-Guel, E. M. Múzquiz-Ramos, J. C. Ríos-Hurtado, A. Moreno-Santos, S. E. Flores-Villaseñor and G. B. Escalante-Ibarra, Surface modification of activated carbon cloth with calcium silicate and hydroxyapatite: bioactive composite material, *Heliyon*, 2022, **8**(11), e11586.
37 L. Black, K. Garbev, P. Stemmermann, K. R. Hallam and G. C. Allen, Characterisation of crystalline C–S–H phases by X-ray photoelectron spectroscopy, *Cem. Concr. Res.*, 2003, **33**(6), 899–911.
38 S. C. Ray, D. K. Mishra, A. M. Strydom and P. Papakonstantinou, Magnetic behavioural change of silane exposed graphene nanoflakes, *J. Appl. Phys.*, 2015, **118**(11), 115302.
39 S. Estrada-Flores, A. Martínez-Luévanos, P. Bartolo-Pérez, L. A. García-Cerda, T. E. Flores-Guía and E. N. Aguilera-González, Facile synthesis of novel calcium silicate hydrated-nylon 6/66 nanocomposites by solution mixing method, *RSC Adv.*, 2018, **8**(73), 41818–41827.
40 H. Idriss, On the wrong assignment of the XPS O 1s signal at 531–532 eV attributed to oxygen vacancies in photo- and electro-catalysts for water splitting and other materials applications, *Surf. Sci.*, 2021, **712**, 121894.
41 F. Esaka, T. Nojima, H. Udono, M. Magara and H. Yamamoto, Non-destructive depth analysis of the surface oxide layer on Mg_2Si with XPS and XAS, *Surf. Interface Anal.*, 2016, **48**(7), 432–435.
42 X. Chen, X. Wang and D. Fang, A review on C 1s XPS-spectra for some kinds of carbon materials, *Fullerenes, Nanotubes Carbon Nanostruct.*, 2020, **28**(12), 1048–1058.
43 Y. Bourlier, M. Bouttemy, O. Patard, P. Gamarra, S. Piotrowicz, J. Vigneron, R. Aubry and S. Delage, Investigation of InAlN layers surface reactivity after thermal annealings: a complete XPS study for HEMT, *ECS J. Solid State Sci. Technol.*, 2018, **7**(6), P329.
44 B. V. Crist, XPS in industry—problems with binding energies in journals and binding energy databases, *J. Electron Spectrosc. Relat. Phenom.*, 2019, **231**, 75–87.
45 K. K. Jani, P. Y. Raval, N. H. Vasoya, M. Nehra, M. Singh, N. Jakhar, S. Kumar, K. B. Modi, D. K. Lim and R. K. Singhal, Impact of Mn^{2+}–Si^{4+} co-substitution on the electronic structure of $Zn_{0.3}Mn_{0.7}Fe_2O_4$ ferrites studied by X-ray photoelectron spectroscopy, *Ceram. Int.*, 2022, **48**(176), 31843–31849.
46 R. Alfonsetti, L. Lozzi, M. Passacantando, P. Picozzi and S. Sanucci, XPS studies on SiO_x thin films, *Appl. Surf. Sci.*, 1993, **70–71**(1), 222–225.
47 H. W. Nesbitt and K. N. Dalby, High resolution O 1s XPS spectral, NMR, and thermodynamic evidence bearing on anionic silicate moieties (units) in PbO-SiO_2 and Na_2O-SiO_2 glasses, *Can. J. Chem.*, 2007, **85**(10), 782–792.
48 S. M. Naga, A. M. Hassan, M. Awaad and F. Bondioli, Influence of Ta_2O_5 doping on the microstructure, physical and mechanical properties of α-alumina ceramics, *J. Ceram. Sci. Technol.*, 2013, **4**(4), 187–192.
49 M. K. Ahmed, S. F. Mansour, R. Al-Wafi, M. Afifi and V. Uskoković, Gold as a dopant in selenium-containing carbonated hydroxyapatite fillers of nanofibrous ε-polycaprolactone scaffolds for tissue engineering, *Int. J. Pharm.*, 2020, **577**, 118950.

50 M. Dehghan, P. Alizadeh and M. Soltani, Investigation of sintering, crystallization and mechanical properties of silver nanoparticles-reinforced wollastonite glass-ceramic, *J. Non-Cryst. Solids*, 2021, **571**, 121028.
51 Y. F. Goh, A. Z. Alshemary, M. Akram, M. R. Adul Kadir and R. Hussain, Bioactive glass: an *in vitro* comparative study of doping with nanoscale copper and silver particles, *Int. J. Appl. Glass Sci.*, 2014, **5**(3), 255–266.
52 Y. Zhang, M. Mizuno, M. Yanagisawa and H. Takadama, Bioactive behaviors of porous apatite- and wollastonite-containing glass-ceramic in two kinds of simulated body fluid, *J. Mater. Res.*, 2003, **18**(2), 433–441.
53 X. Liu, C. Ding and P. K. Chu, Mechanism of apatite formation on wollastonite coatings in simulated body fluids, *Biomaterials*, 2004, **25**(10), 1755–1761.
54 K. R. Mohamed, S. M. Mousa and G. T. El-Bassyouni, Fabrication of nano structural biphasic materials from phosphogypsum waste and their *in vitro* applications, *Mater. Res. Bull.*, 2014, **50**, 432–439.
55 Q. Lin, X. Lan, Y. Li, Y. Ni, C. Lu, Y. Chen and Z. Xu, Preparation and *in vitro* bioactivity of zinc incorporating tricalium silicate, *Mater. Sci. Eng., C*, 2011, **31**(3), 629–636.
56 S. V. Dorozhkin, There are over 60 ways to produce biocompatible calcium orthophosphate ($CaPO_4$) deposits on various substrates, *J. Compos. Sci.*, 2023, **7**(7), 273.
57 X. Cheng, D. Li and R. Cui, Introducing a novel therapeutic supplement for osteoporosis: remedial, cytotoxicity and antioxidant effects of plant extract green-formulated gold nanoparticles, *J. Eng. Res.*, 2024, **12**(1), 9–16.
58 B. Sheng, Y. P. Chu, W. T. Wong, E. K. C. Yau, S. P. L. Chen and W. H. Luk, Improvement of bone mineral density after enzyme replacement therapy in Chinese late-onset Pompe disease patients, *BMC Res. Notes*, 2017, **10**(1), 351.
59 K. I. Nakahama, Cellular communications in bone homeostasis and repair, *Cell. Mol. Life Sci.*, 2010, **67**(23), 4001–4009.
60 H. Lin, Y. Tang, T. P. Lozito, N. Oyster, B. Wang and R. S. Tuan, Efficient *in vivo* bone formation by BMP-2 engineered human mesenchymal stem cells encapsulated in a projection stereolithographically fabricated hydrogel scaffold, *Stem Cell Res. Ther.*, 2019, **10**(1), 254.
61 D. H. Yang, H. Nah, D. Lee, S. J. Min, S. Park, S. H. An, J. Wang, H. Hee, K. S. Choi, W. K. Ko, J. S. Lee, I. K. Kwon, S. J. Lee and D. N. Heo, A review on gold nanoparticles as an innovative therapeutic cue in bone tissue engineering: prospects and future clinical applications, *Mater Today Bio*, 2024, **26**, 101016.
62 C. Ren, W. Gong, F. Li and M. Xie, Pilose antler aqueous extract promotes the proliferation and osteogenic differentiation of bone marrow mesenchymal stem cells by stimulating the BMP-2/Smad1, 5/Runx2 signaling pathway, *Chin. J. Nat. Med.*, 2019, **17**(10), 756–767.
63 A. A. Mostafa, M. M. El-Sayed, A. N. Emam, A. A. Abd-Rabou, R. M. Dawood and H. Oudadesse, Bioactive glass doped with noble metal nanoparticles for bone regeneration: *in vitro* kinetics and proliferative impact on human bone cell line, *RSC Adv.*, 2021, **11**, 25628–25638.
64 Y. Shi, X. Han, S. Pan, Y. Wu, Y. Jiang, J. Lin, Y. Chen and H. Jin, Gold nanomaterials and bone/cartilage tissue engineering: biomedical applications and molecular mechanisms, *Front. Chem.*, 2021, **9**, 724188.
65 E. Beurel, S. F. Grieco and R. S. Jope, Glycogen synthase kinase-3 (GSK3): regulation, actions, and diseases, *Pharmacol. Ther.*, 2015, **148**, 114–131.
66 M. Arioka and F. Takahashi-Yanaga, Glycogen synthase kinase-3 inhibitor as a multi-targeting anti-rheumatoid drug, *Biochem. Pharmacol.*, 2019, **165**, 207–213.
67 E. M. AbouZeid, A. H. Afifi, A. Salama, R. A. Hussein, F. S. Youssef, S. H. El-Ahmady and N. M. Ammar, Comprehensive metabolite profiling of Phoenix rupicola pulp and seeds using UPLC-ESI-MS/MS and evaluation of their estrogenic activity in ovariectomized rat model, *Food Res. Int.*, 2022, **157**, 111308.
68 X. Cheng, D. Li and R. Cui, Introducing a novel therapeutic supplement for osteoporosis: remedial, cytotoxicity and antioxidant effects of plant extract green-formulated gold nanoparticles, *J. Eng. Res.*, 2024, **12**(1), 9–16.
69 S. V. Dorozhkin, Bioceramics of calcium orthophosphates, *Biomaterials*, 2010, **31**(7), 1465–1485.
70 M. Wang, Developing bioactive composite materials for tissue replacement, *Biomaterials*, 2003, **24**(13), 2133–2151.
71 B. Ekram, S. M. Mousa, G. T. El-Bassyouni, B. M. Abdel-Hady and M. Moaness, Novel Highly Proliferative Electrospun Cerium-Doped Hydroxyapatite/Polyamide/Gelatin Nanofibers for Guided Bone Regeneration Application, *Mater. Chem. Phys.*, 2025, **342**, 130975.
72 R. H. Lin, H. S. Hung, C. M. Tang, H. K. Tsou, P. H. Chen, C. Y. Yueh and H. M. D. Wang, *In vitro* biocompatibility of polycaprolactone/hydroxyapatite nanocomposite membranes modified by oleic acid for bone regeneration, *Colloids Surf., A*, 2024, **688**, 133576.
73 L. L. Hench, The story of Bioglass®, *J. Mater. Sci.:Mater. Med.*, 2006, **17**(11), 967–978.
74 I. D. Xynos, M. V. J. Hukkanen, J. J. Batten, L. D. Buttery, L. L. Hench and J. M. Polak, Bioglass® 45S5 stimulates osteoblast turnover and enhances bone formation in vitro: implications and applications for bone tissue engineering, *Calcif. Tissue Int.*, 2000, **67**, 321–329.
75 D. Zhang, D. Liu, J. Zhang, C. Fong and M. Yang, Gold nanoparticles stimulate differentiation and mineralization of primary osteoblasts through the ERK/MAPK signaling pathway, *Mater. Sci. Eng., C*, 2014, **42**, 70–77.
76 F. Rupp, R. A. Gittens, L. Scheideler, A. Marmur, B. D. Boyan, Z. Schwartz and J. Geis-Gerstorfer, A review on the wettability of dental implant surfaces I: theoretical and experimental aspects, *Acta Biomater.*, 2014, **10**(7), 2894–2906.